Joule

CellPress

Article

Discovery of the Zintl-phosphide $BaCd_2P_2$ as a long carrier lifetime and stable solar absorber

Zhenkun Yuan,[1,10] Diana Dahliah,[2,3,10] Muhammad Rubaiat Hasan,[4] Gideon Kassa,[1] Andrew Pike,[1] Shaham Quadir,[5] Romain Claes,[2] Cierra Chandler,[6] Yihuang Xiong,[1] Victoria Kyveryga,[4,7] Philip Yox,[4,7] Gian-Marco Rignanese,[2] Ismaila Dabo,[6] Andriy Zakutayev,[5] David P. Fenning,[8] Obadiah G. Reid,[5,9] Sage Bauers,[5] Jifeng Liu,[1] Kirill Kovnir,[4,7] and Geoffroy Hautier[1,11,*]

SUMMARY

Thin-film photovoltaics (PV) offers a path to decarbonize global energy production. Unfortunately, existing thin-film solar absorbers have major issues associated with either elemental abundance, stability, or performance. Entirely new and disruptive materials platforms are rarely discovered, and their search is traditionally slow and serendipitous. Here, we report a first-principles high-throughput (HT) computational screening for new solar absorbers among 40,000 known inorganic materials. Next to band gap and carrier effective masses, we also use computed intrinsic defects as they can limit the carrier lifetime. We identify the Zintl-phosphide $BaCd_2P_2$ as a potential high-efficiency solar absorber. Follow-up experiments confirm the promises of $BaCd_2P_2$, highlighting an optimal band gap, bright photoluminescence (PL), and long carrier lifetime, even in unoptimized powder samples. Importantly, $BaCd_2P_2$ contains no critical elements and is stable in air and water. Our work demonstrates how computational screening combined with experiments can accelerate the search for photovoltaic materials.

INTRODUCTION

Photovoltaics (PV) will play a central role in the ongoing energy transition toward a sustainable, low-carbon-emission society.[1–3] In that regard, thin-film solar cells have remarkable prospects because their manufacturing can require smaller upfront capital investment, less energy input, and produce fewer greenhouse gas emissions than today's dominant silicon-based technology.[4] Thin-film technologies can also offer compatibility with flexible substrates and band-gap tuning opportunities, leading to building-integrated power generation or tandem devices in combination with silicon PV.[5–7] Among the different materials used as solar cell absorbers, CdTe and $Cu(In,Ga)Se_2$ (CIGS) have achieved high power conversion efficiency of over 22% and have been commercialized for almost two decades.[8,9] Unfortunately, CdTe and CIGS rely on critical elements, such as tellurium and indium, raising concerns for multi-terawatt scale deployment.[10,11] Over the last decade, earth-abundant thin-film materials such as $Cu_2ZnSn(S,Se)_4$ (CZTS) and, in particular, lead halide perovskites (e.g., $MAPbI_3$, where MA = $CH_3NH_3^+$) have emerged. However, CZTS lags behind commercial thin-film technologies in efficiency,[12–14] while halide perovskites suffer from long-term stability issues.[15–20]

Large-scale deployment of thin-film PV demands high-efficiency, stable, and low-cost solar absorbers that are yet to be discovered. For over half a century, only a

CONTEXT & SCALE

Thin-film PV provides a path to carbon-free electricity generation. However, existing thin-film solar absorbers have major issues associated with either elemental abundance, stability, or performance, limiting large-scale deployment of thin-film PV. Here, we use computational screening to search for new solar absorbers among 40,000 known inorganic materials. Because point defects are known to promote carrier recombination (and losses), we include them in the screening. We computationally discover a promising low-cost solar absorber, the Zintl-phosphide $BaCd_2P_2$, and confirm its properties experimentally. This material combines attractive optoelectronic properties with slow carrier recombination and high stability. Our work not only opens an avenue for a new class of thin-film solar absorbers but also demonstrates how computational screening combined with experiments can accelerate the search for PV materials, moving the field away from serendipitous materials discovery.

Yuan et al., Joule 8, 1–18
May 15, 2024 © 2024 Elsevier Inc.
https://doi.org/10.1016/j.joule.2024.02.017

limited number of materials have been explored for thin-film PV applications,[21–27] as conventional materials discovery is an intrinsically slow process. Most of the materials research efforts in the thin-film PV field have been devoted to modifying known semiconductors (cation substitution in CZTS,[28–32] mixed-cation/mixed-halide perovskites,[33–36] etc.), but the recent advent of halide perovskites demonstrates that an unexpected new family of PV materials can still be found and revolutionize the field. This motivates further "out-of-the-box" explorative work, especially toward more stable materials than the halide perovskites.

High-throughput (HT) computational screening can significantly accelerate materials discovery and is emerging in the PV field.[37–48] Although earlier HT searches for solar absorbers focused on bulk material properties, such as band gap, effective mass, and optical absorption coefficient,[37–46] more complex properties related to intrinsic defects have started to be integrated into the screening as well.[47,48] Considering defect-assisted nonradiative carrier recombination is essential in the search for new high-performance solar absorbers.[49,50] Indeed, designing and discovering materials with "defect tolerance" and long carrier lifetime has become an important target for the PV community.[50–56] Yet, only a few HT studies have included defect properties in the screening process, and their focus so far was on copper-based inorganic materials[47] and perovskite compounds.[48] Moreover, these computational predictions have not yet led to the experimental realization of a proposed solar absorber.

Here, we identify the $BaCd_2P_2$ as a long carrier lifetime and stable solar absorber using HT computational screening followed by bulk synthesis and experimental characterization. We perform an HT search to screen about 40,000 inorganic materials obtained from the Materials Project database,[57] most of which are registered in the Inorganic Crystal Structure Database (ICSD).[58] We find a handful of materials combining a suitable band gap, small effective masses, and promising defect properties that will not cause strong nonradiative carrier recombination. Among these promising candidates, we select the Zintl-phosphide $BaCd_2P_2$ and explicitly show that the computed nonradiative recombination rates in $BaCd_2P_2$ are better than or comparable with those in high-efficiency solar absorbers such as the halide perovskites. We experimentally synthesize and characterize $BaCd_2P_2$, showing that this material is highly stable in air and water. Bright photoluminescence (PL) and time-resolved microwave conductivity (TRMC) measurements confirm the computed direct band gap of 1.45 eV and present a promising long carrier lifetime of up to 30 ns. All of these results indicate that $BaCd_2P_2$ is a promising high-performance solar cell absorber with the potential to open a new avenue in PV for an entire family of Zintl AM_2X_2 solar absorbers (where A and M are +2 ions and X is a pnictogen).

RESULTS

HT computational identification of $BaCd_2P_2$

Our starting point is the Materials Project electronic structure database. Without constraints on any specific chemistry, we obtain 39,659 materials with full data on crystal structure, electronic band structure, and effective masses. We adopt a tiered computational screening approach (very similar to our previous work[47]) to search for solar cell absorbers among these materials. The procedure is detailed in Note S1 of the supplemental information. Including electronic and defect properties in HT screening requires combining calculations at different levels of theory from (semilocal) density functional theory (DFT) to more accurate, but computationally expensive, Heyd-Scuseria-Ernzerhof (HSE) hybrid functional.[59] Our screening consists of

[1]Thayer School of Engineering, Dartmouth College, Hanover, NH 03755, USA

[2]Institute of Condensed Matter and Nanosciences, Université Catholique de Louvain, Chemin des Étoiles 8, 1348 Louvain-la-Neuve, Belgium

[3]Department of Physics, An-Najah National University, Nablus, Palestine

[4]Department of Chemistry, Iowa State University, Ames, IA 50011, USA

[5]National Renewable Energy Laboratory, Golden, CO 80401, USA

[6]Department of Materials Science and Engineering, Materials Research Institute, The Pennsylvania State University, University Park, PA 16802, USA

[7]Ames National Laboratory, U.S. Department of Energy, Ames, IA 50011, USA

[8]Department of Nanoengineering, University of California, San Diego, La Jolla, CA 92093, USA

[9]Renewable and Sustainable Energy Institute, University of Colorado, Boulder, Boulder, CO 80309, USA

[10]These authors contributed equally

[11]Lead contact

*Correspondence: geoffroy.hautier@dartmouth.edu

https://doi.org/10.1016/j.joule.2024.02.017

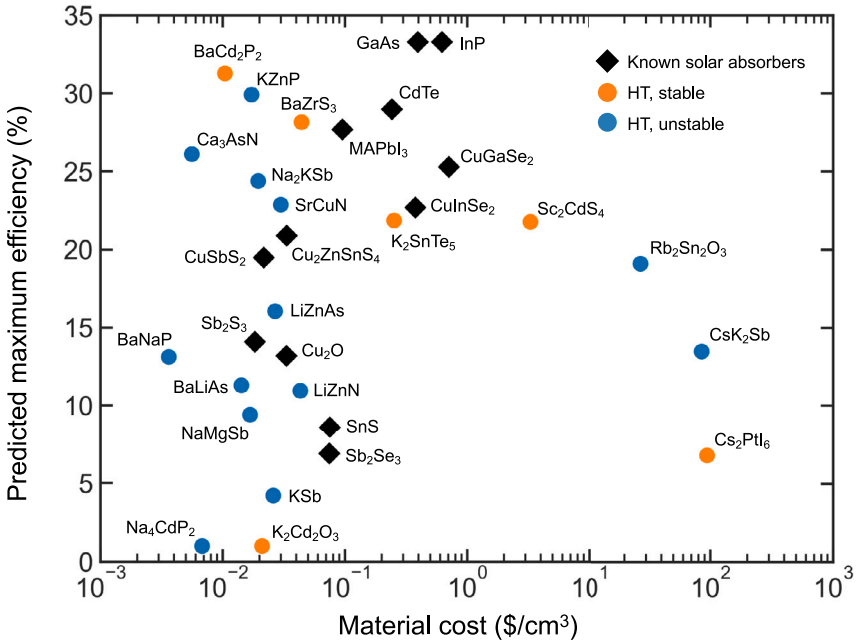

Figure 1. Theoretical power conversion efficiency versus material cost for 19 potential thin-film solar cell absorbers identified from high-throughput (HT) screening

Black diamonds represent known thin-film solar absorbers for comparison purposes. Orange circles represent materials that are probably stable in air and moisture. Blue circles represent materials that are likely to be sensitive to air and moisture. Details on the stability assessment are available in Table S1 of supplemental information.

considering first DFT band gaps and effective masses, followed by a refinement of the band gap using the HSE hybrid functional, and then defect computations combining DFT and HSE. Finally, we perform full HSE defect calculations for 19 candidates and predict their solar-cell efficiency using an extended detailed-balance (i.e., Shockley-Queisser) model, which accounts for defect-assisted nonradiative carrier recombination.[47,60–62] At this screening stage, we examine only vacancies and cation-cation antisites without considering interstitials and cation-anion antisites. For nonradiative recombination, we assume a constant carrier capture cross-section for all defects. This effectively penalizes materials with low-formation-energy, deep defects. Previous work has shown that this model can discriminate between high-performance solar absorbers and materials that are unlikely to realize high efficiency because of their defect properties.[47,60–62] The 19 candidates, together with 12 established solar absorbers, are displayed in Figure 1 with their theoretical power conversion efficiency and estimated material cost (see Note S1 for more details). Additional metrics (beyond cost) related to elemental supply risks can be found in Figure S2. Given that stability issues are hampering the deployment of halide perovskite solar cells, we have taken into account stability in selecting candidate materials. Unfortunately, there is no easy-to-compute criterion for assessing stability in realistic conditions. We can estimate the thermodynamic stability (energy above hull) of material versus competing phases from DFT, but this is a poor indicator of stability in air and with respect to moisture.[63,64] In fact, most non-oxide materials show thermodynamic instability in contact with oxygen.[65] Kinetic effects and surface passivation are likely to be key factors for their stability but are currently poorly assessed by theory. To assess the stability of the candidate materials, we therefore follow the experimental reports on these materials, including the work reporting their synthesis and structural determination. As summarized in Table S1, direct experimental

information on air/moisture stability can be found for most of the candidate materials. Interestingly, the reported air/moisture stabilities agree with the solid-state-chemistry experience of the authors: the higher the alkali and alkaline-earth metal per formula unit, the less stable to air/moisture the material will likely be. For example, according to this experience, KZnP (33%) should be less stable than $BaCd_2P_2$ (20%), which is in line with the experiment. For BaLiAs, BaNaP, KSb, and Na_4CdP_2, which to our knowledge lack direct experimental information on air/moisture stability, we expect them to be highly sensitive to air/moisture, given their high alkali and alkaline-earth metal per formula unit. Our stability assessment is conveyed in Figure 1 through the color of the data point.

The most promising candidates when combining power conversion efficiency, material cost, and stability are $BaCd_2P_2$ and $BaZrS_3$. The $BaZrS_3$ perovskite has recently been studied for thin-film PV applications.[66,67] In contrast, $BaCd_2P_2$ is classified as a Zintl compound and has received little attention in the PV field since it was experimentally reported in the 1980s.[68] Although $BaCd_2P_2$ has recently been shown to possess a suitable band gap and small effective masses,[43,69] our HT screening, which includes defect-assisted nonradiative recombination, makes it stand out from the vast number of materials with suitable band gaps. Other candidates, such as the spinel $ScCd_2S_4$ or K_2SnTe_5, have cost and abundance issues. They are still of scientific interest, and substitution strategies could be considered to reduce or even eliminate the use of the critical elements (Sc and Te). Other interesting candidates, such as KZnP, Na_2KSb, SrCuN, and Ca_3AsN, are excluded due to stability concerns, confirmed by their experimental synthesis reports.[70–74] Based on these considerations, we select $BaCd_2P_2$ as the most promising solar absorber candidate. In the following, we provide a more detailed study of the optoelectronic and defect properties of $BaCd_2P_2$.

$BaCd_2P_2$ computed bulk optoelectronic properties

$BaCd_2P_2$ crystallizes in the $P\bar{3}m1$ $CaAl_2Si_2$ Zintl-type structure[68,75] (Figure 2A). The crystal structure consists of alternating layers of tetrahedrally coordinated Cd and octahedrally coordinated Ba. This structure type has attracted substantial interest for thermoelectric applications, e.g., the antimonides Mg_3Sb_2 and $CaMg_2Sb_2$.[76] Figure 2B shows the $BaCd_2P_2$ band structure calculated with HSE. The direct band gap value of 1.45 eV is ideal for single-junction solar cells according to the detailed-balance model. There is a competing indirect gap that should not be detrimental to PV performance and, instead, has been suggested to be beneficial to carrier lifetime.[77] The band structure exhibits dispersive valence and conduction bands. As a result, the effective masses are low for both electrons (0.11–0.74 m_0) and holes (0.44–0.63 m_0).[57,78] Further carrier mobility calculations including phonon scattering give a room-temperature mobility of 111–916 cm^2/Vs for electrons and 123–242 cm^2/Vs for holes, depending on the crystallographic direction (Figure S3). The computed mobility is for a perfect single crystal of $BaCd_2P_2$ and provides an upper bound for the mobilities in a polycrystalline film with impurities. Although lower than in III-V semiconductors such as GaAs, the mobilities are comparable with those in many other solar absorbers such as CdTe,[79,80] CZTS,[81] and $MAPI_3$.[82] Besides, as shown in Figure 2C, the computed optical absorption coefficient of $BaCd_2P_2$ is over 10^4 cm^{-1} in the visible light range and is on par with those of known thin-film solar absorbers.

$BaCd_2P_2$ defect charge transition levels and dopability

Our HT screening has identified $BaCd_2P_2$ to be of interest, not only for its band gap, carrier transport, and optical absorption but also for the absence of low-formation-energy, deep defects that can act as strong nonradiative recombination centers. In

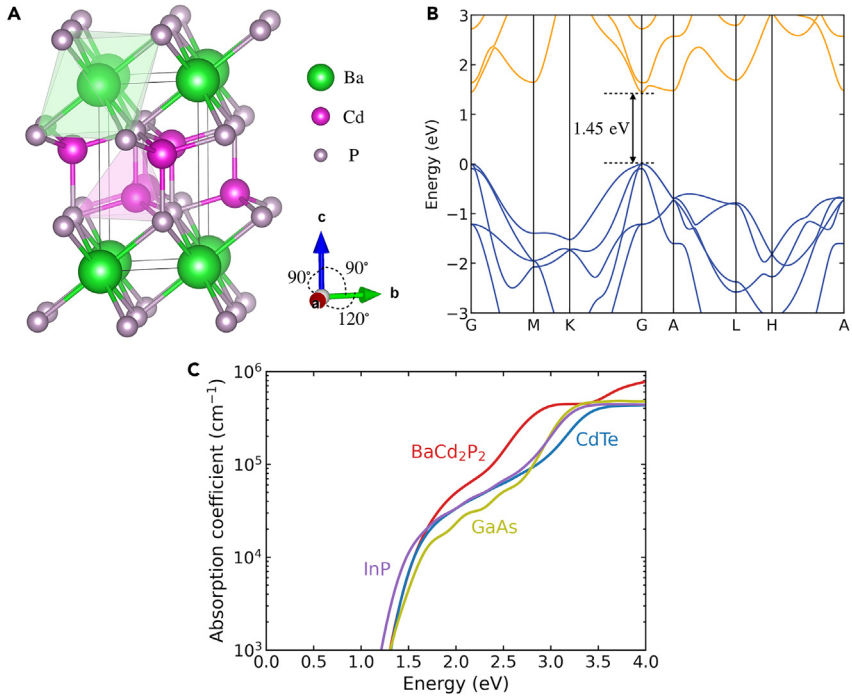

Figure 2. Crystal structure, electronic band structure, and optical absorption of $BaCd_2P_2$

(A) Crystal structure of $BaCd_2P_2$. Green octahedra and pink tetrahedra show the phosphorus coordination of Ba and Cd, respectively.

(B) HSE electronic band structure of $BaCd_2P_2$.

(C) Calculated optical absorption spectra of $BaCd_2P_2$. The absorption calculation is at the DFT-GGA-PBE level, with the band gap corrected using the HSE value. Also shown are the calculated optical absorption spectra for GaAs, CdTe, and InP at the same level of theory.

the initial screening, we considered only limited types of intrinsic point defects. In the following, we provide a comprehensive first-principles study of intrinsic point defects in $BaCd_2P_2$. The electrical behavior of the defects is assessed based on their calculated formation energies and charge transition levels. The defect formation energy depends on the elemental chemical potentials that are related to synthesis conditions. The allowed chemical potentials of Ba, Cd, and P satisfy the stability condition of $BaCd_2P_2$ and are bound by the formation of different secondary phases in the Ba-Cd-P system (see Figure S4). Figures 3A and 3B plot the defect formation energies as a function of Fermi level under P-poor and P-rich conditions (Figure S4), respectively. Formation energies at other chemical-potential conditions can be found in Figure S5.

Figures 3A and 3B show that vacancies are the dominant defect species in $BaCd_2P_2$: V_{Ba} and V_{Cd} are the dominant acceptors; V_P is the dominant donor. When ionized, the vacancies can have low formation energies for Fermi-level positions close to the respective band edges. Fortunately, they are all shallow defects and can therefore be ruled out as nonradiative recombination centers. Early on in the study of lead halide perovskites, it was hypothesized that the long carrier lifetime and defect tolerance of $MAPI_3$ result from the shallow nature of vacancy defects.[83,84] Although for $MAPI_3$ this picture has been challenged by recent studies,[85–88] $BaCd_2P_2$ clearly shows shallow vacancies for both cations and anions. The formation of shallow vacancies has been linked to the electronic structure of the material and, more specifically, to the presence of an antibonding upper valence band and a bonding lower

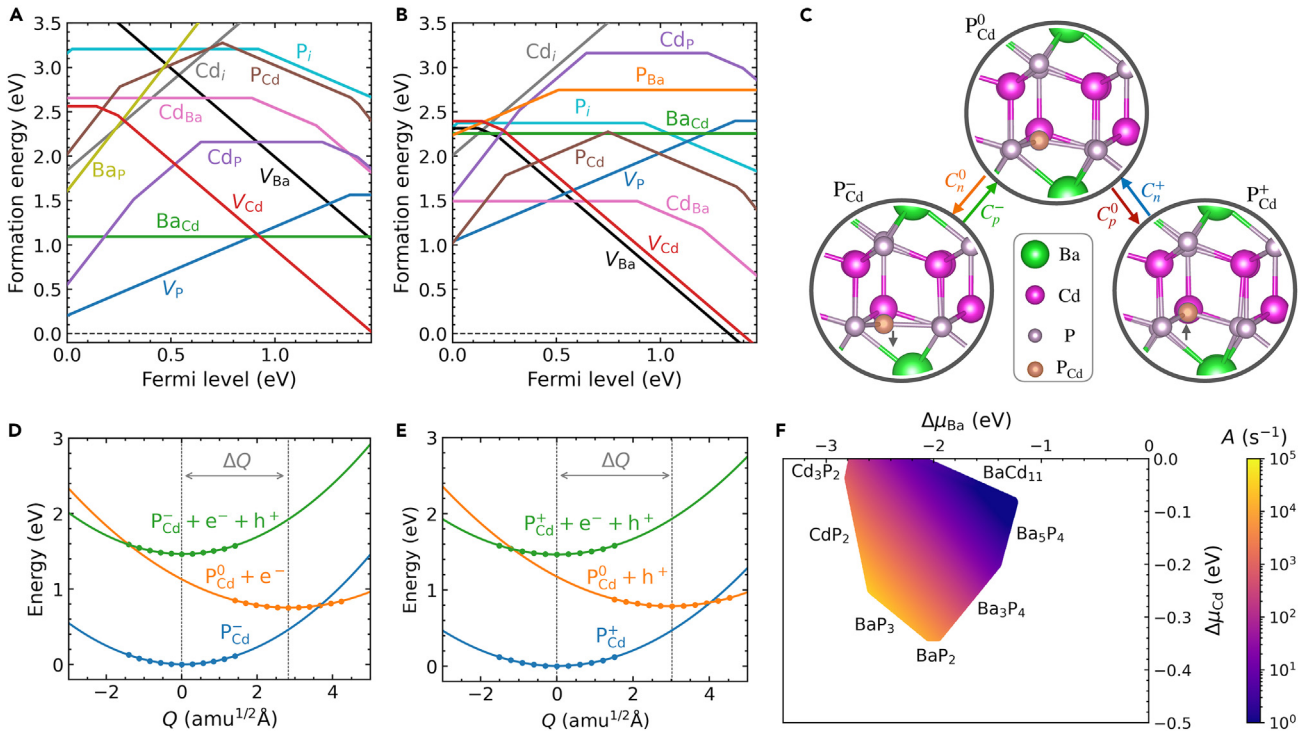

Figure 3. Formation energies of intrinsic point defects, carrier capture at the P_{Cd} antisite, and nonradiative carrier recombination in $BaCd_2P_2$

(A and B) HSE-calculated defect formation energies as a function of Fermi level under P-poor and P-rich conditions, respectively. The formation energies of Ba interstitials (Ba$_i$) are out of the y axis range of the plots and are therefore not visible.

(C) Local atomic structures of the P_{Cd} antisite in the 0, −1, and +1 charge states (see also Figure S8D). The gray arrows indicate the relaxation of the phosphorus antisite when charged. Transition between two adjacent charge states involves two carrier capture processes, as indicated by the colored arrows and the corresponding capture coefficients; for the capture coefficients, the superscript denotes the initial charge state and the subscript denotes the carrier type (*n*, electron; *p*, hole).

(D and E) Configuration coordinate diagrams describing the P_{Cd} (0/−) and (0/+) charge-state transitions, respectively (see also Figures S8A and S8B).

(F) Nonradiative recombination rate (denoted as *A*, in unit of s^{-1}) in intrinsic $BaCd_2P_2$ as a function of elemental chemical potentials in the ($\Delta\mu_{Ba}$, $\Delta\mu_{Cd}$) plane. The *A* rates are given by $A = C_{tot} \times N_d$. Here, only the dominant nonradiative center P_{Cd} is considered. The defect density (N_d) of P_{Cd} is computed at 1,000 K considering the high synthesis temperature of $BaCd_2P_2$ (Note S3), while the total capture coefficient (C_{tot}) of P_{Cd} is determined at 300 K.

conduction band.[51,53,89] It has been argued that this type of bonding pushes up the valence-band maximum (VBM) and pushes down the conduction-band minimum (CBM), making the band edges close to the vacancy dangling-bond states and hence leading to shallow vacancy defect levels. This defect-tolerant electronic structure concept applies partially to $BaCd_2P_2$; that is, for $BaCd_2P_2$, the upper valence band consists of antibonding states between Cd 4*d* and P 3*p*, while the lower conduction band arises mostly from the antibonding interactions between Cd 5*s* and P 3s and 3p (Figure S6). In this regard, $BaCd_2P_2$ is similar to $MAPI_3$, where both the upper valence band and lower conduction band are antibonding (Pb 6*s*-I 5*p* and Pb 6*p*-I 5*p*, respectively).[50,52,55]

Some of the antisite defects in $BaCd_2P_2$ can also be low in formation energy, notably for Ba_{Cd} and Cd_{Ba}. Given the large difference in ionic radii between Cd^{2+} and Ba^{2+} (1.09 versus 1.49 Å), one would expect that it should be energetically unfavorable to form Ba_{Cd} than Cd_{Ba}. However, our previous analysis has shown no clear correlation between ionic size difference and antisite formation energy.[47] What our previous study found, however, is that elements with similar preferred oxidation states tend not to form antisites with deep levels. This is the case here for Ba occupying the site of the smaller Cd but, surprisingly, not for Cd replacing the larger Ba. The

Ba_{Cd} introduces no defect level in the band gap of $BaCd_2P_2$, as expected. By contrast, Cd_{Ba} is a deep double acceptor. This may be understood from the larger antisite space of Cd_{Ba}, in which not only Cd^{2+} but also Cd^{+} and Cd^{0} with bigger ionic sizes can form. Both the P_{Cd} and Cd_P antisites are amphoteric (i.e., exhibiting both positive and negative charge states across the band gap[90]) and have deep levels in the band gap. The amphoteric behavior of these two antisites may be linked to the oxidation behavior of P, which can act both as a cation and anion and has oxidation states spanning from +5 to −3. The interstitials (P_i, Cd_i, and especially Ba_i) have overall high formation energies and should not be a concern for nonradiative carrier recombination. Based on these results, we will later assess quantitatively the effectiveness of Cd_{Ba}, P_{Cd}, and Cd_P as nonradiative recombination centers. We note that cation-anion antisites have also been found to form deep defects in other phosphide solar absorbers, such as InP[91] and Zn_3P_2.[92]

The defect formation energies plotted in Figures 3A, 3B, and S5 provide important insights into doping in $BaCd_2P_2$. Irrespective of the elemental chemical potentials, $BaCd_2P_2$ clearly will not be highly doped, either p-type or n-type, by the intrinsic point defects. The equilibrium Fermi-level position, which can be estimated to be near the crossing point between the formation-energy curves for the dominant acceptor and donor species (such as V_{Cd} and V_P in Figure 3A), never gets close to the band edges, implying very low free carrier concentration. Extrinsic acceptor doping could potentially make $BaCd_2P_2$ p-type doped, especially under the P-rich condition, where the V_P donor and other donor defects have overall high formation energies, meaning weak compensation (Figure 3B). In contrast, n-type doping in $BaCd_2P_2$ is likely to be challenging due to strong compensation from V_{Ba} and V_{Cd}, whose formation energies can drop to nearly or even below zero for Fermi-level positions close to the CBM. This doping asymmetry agrees with the relatively high absolute energy of the valence-band edge of $BaCd_2P_2$ (see Table S2).[93,94] We conclude that $BaCd_2P_2$ is a natively semi-insulating material with high potential of realizing good p-type doping. It could be used as an intrinsic layer in a p-i-n junction or as a p-type layer in a p-n junction.

Deep defects and nonradiative recombination in $BaCd_2P_2$

Strong nonradiative carrier recombination requires deep defects with a high enough concentration but also large carrier capture coefficients.[95–97] From the above (Figures 3A and 3B), the deep defects with low formation energies are Cd_{Ba}, P_{Cd}, and Cd_P. The capture coefficients can be calculated from first principles, considering nonradiative transition between the deep defect level and an electron at the CBM or a hole at the VBM via multiphonon emission (details in Note S2). Here, we calculate capture coefficients for Cd_{Ba}, P_{Cd}, and Cd_P and determine nonradiative carrier recombination rates in $BaCd_2P_2$. We assume an intrinsic $BaCd_2P_2$ absorber layer in a p-i-n device.

The Cd_{Ba} gives rise to a deep (0/−) level at 0.89 eV above the valence band (Figures 3A and 3B). However, the configuration coordinate diagram for Cd_{Ba} (0/−) transition indicates that the electron capture barrier by Cd_{Ba}^{0} and the hole capture barrier by Cd_{Ba}^{-} are both large (Figure S7A). Therefore, without explicitly computing the capture coefficients, Cd_{Ba} should not be a strong recombination center despite being a deep-level defect. The P_{Cd} has a (+/−) transition level near the mid gap. The direct transition between −1 and +1 states will not be efficient due to the low probability of a defect capturing two electrons (or two holes) at once.[98] The recombination process of P_{Cd} can be treated by including the unstable neutral charge state ($q = 0$) and through two steps involving the (0/−) and (0/+) transition

levels, as previously done for the iodine interstitial (I_i) in $MAPI_3$.[99] This amounts to four capture processes and coefficients in total: C_n^0 and C_n^+ for electron (n) capture and C_p^0 and C_p^- for hole (p) capture, as shown in Figure 3C. The P_{Cd} (0/−) and (0/+) levels are also very deep and locate 0.71 and 0.78 eV above the VBM, respectively (Figures S8A and S8B). Figures 3D and 3E show the configuration coordinate diagrams for the P_{Cd} (0/−) and (0/+) transitions, respectively. All four capture processes have small energy barriers, which qualitatively indicates that the capture processes by P_{Cd} can be easy. Quantitatively, for P_{Cd}, our calculations—including electron-phonon coupling—yield a total capture coefficient (C_{tot}) of 2.77×10^{-7} cm^3/s at 300 K (see Figure S8C), which is significant but comparable with that of the most active recombination center (I_i) in $MAPI_3$.[97,99] The local atomic structures of P_{Cd}^0, P_{Cd}^-, and P_{Cd}^+ plotted in Figure 3C highlight large displacements of the phosphorus antisite as a result of the charge transitions: the electron (hole) capture by P_{Cd}^0 leads to a downward (upward) displacement of the phosphorus antisite, and P_{Cd}^- (P_{Cd}^+) shows a trigonal planar (trigonal pyramidal) P_4 configuration with three equidistant P–P bonds. The Cd_P antisite gives rise to a deep (0/2+) level in the band gap. Compared with P_{Cd}, Cd_P presents a negligibly small C_{tot} at 300 K, mainly due to large hole capture barriers (Figures S7B and S7C; Table S4).

The above results indicate that P_{Cd} is the most efficient nonradiative recombination center in $BaCd_2P_2$, followed by Cd_P, and that Cd_{Ba} is inactive. In the following, we determine the nonradiative recombination rates in intrinsic $BaCd_2P_2$ at 300 K (see Note S2). The nonradiative recombination rate (denoted as A) is given by $A = C_{tot} \times N_d$, where C_{tot} and N_d are the total capture coefficient and concentration of a recombination center, respectively. Figure 3F plots the nonradiative recombination rate A in intrinsic $BaCd_2P_2$ as a function of the elemental chemical potentials that control defect formation energy and concentration. The recombination rate is larger under P-rich conditions, which favor the formation of P_{Cd}. Remarkably, the recombination rate is at most $\sim10^5$ s^{-1}, which is orders of magnitude smaller than that of $MAPI_3$ ($\sim10^7$ s^{-1}, computed at a similar level of theory).[97,99] This is because the P_{Cd} concentration is rather low (on the order of 10^{11} cm^{-3} or less) in intrinsic $BaCd_2P_2$. Indeed, the lowest formation energy of P_{Cd}, even under the extreme P-rich condition, is higher than 1.0 eV (Figure 3B), which is still larger than the highest formation energy of the I_i in $MAPI_3$ under the iodine-rich condition.[99] We also emphasize that the C_{tot} of P_{Cd} is comparable with that of I_i in $MAPbI_3$. Using the calculated A rates, the nonradiative lifetime ($= 1/A$) in intrinsic $BaCd_2P_2$ is on the order of at least 10 μs, indicating the potential for a remarkably long bulk carrier lifetime.

If $BaCd_2P_2$ is used as a p-type absorber layer in a p-n junction, the carrier capture behavior changes. In p-type $BaCd_2P_2$, the electron capture coefficients will dominate the total capture coefficient (Note S2; Table S4). As a consequence, not only P_{Cd} but also Cd_P will act as nonradiative centers. In addition, the P_{Cd} and Cd_P concentrations will be orders of magnitude higher when the Fermi level gets closer to the valence band (Figures 3A and 3B). Assuming that the Fermi level is 0.2 eV above the VBM, the nonradiative recombination rates are $\sim10^6$–10^8 s^{-1} (Figure S9). Such values are still on par with those in standard inorganic p-type solar absorbers CdTe,[100,101] CIGS,[102] and CZTS,[103,104] where the computed A rates of $\sim10^7$ s^{-1} have been typically reported.

Synthesis and stability of $BaCd_2P_2$

All our computational results (band gap, optical absorption, carrier mobilities, intrinsic point defects, and nonradiative carrier recombination at deep defects) highlight $BaCd_2P_2$ as a potentially high-performance inorganic solar absorber made of

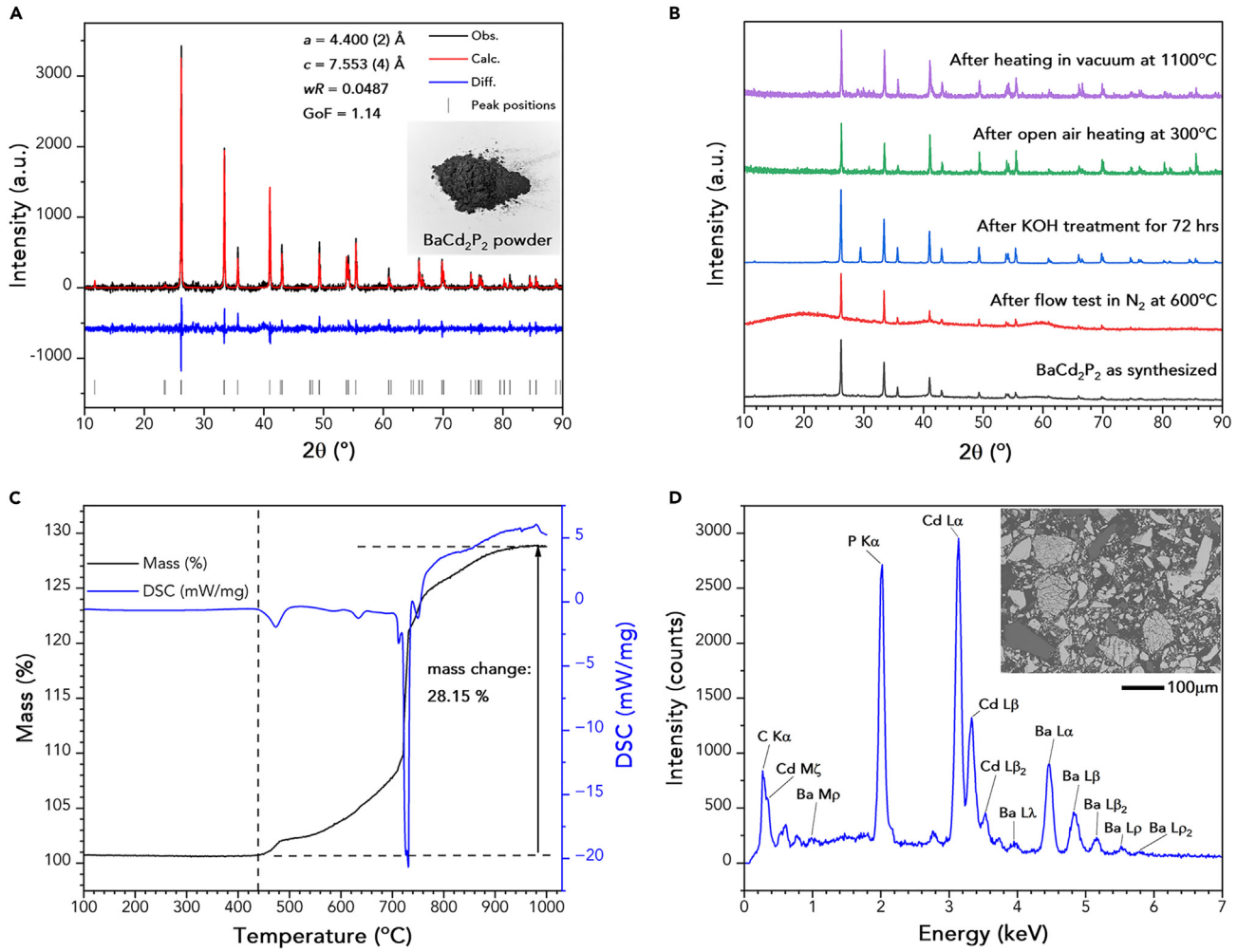

Figure 4. Characterization of crystal structure and phase stability of $BaCd_2P_2$ polycrystalline sample

(A) PXRD pattern with Rietveld refinement for as-synthesized $BaCd_2P_2$ sample.

(B) PXRD patterns of the $BaCd_2P_2$ samples after stability tests under various conditions.

(C) TGA and DSC analyses of the thermal behavior of $BaCd_2P_2$ in air atmosphere.

(D) Representative EDS spectra of $BaCd_2P_2$ with SEM image (scale bar, 100 μm).

low-cost elements. $BaCd_2P_2$ was reported experimentally,[68] but no experimental characterization of the optoelectronic properties of this material had been made. We have synthesized $BaCd_2P_2$ powder samples by solid-state reaction of the elemental Ba, Cd, and P in stoichiometric ratio in sealed silica ampoules. Details about the synthesis and characterization of the crystal structure and phase stability are provided in Notes S3–S6 of the supplemental information. Figure 4A plots the powder X-ray diffraction (PXRD) pattern of the $BaCd_2P_2$ sample, which shows no coexistence of secondary phases and confirms the previously reported crystal structure. The crystal lattice parameters obtained from PXRD Rietveld refinement agree well with previous measurements and our calculations (see Table S5).

As highlighted by halide perovskites, whose applications are limited by their stability,[15–20] air- and moisture-sensitivity has become an important concern for the technological deployment of new solar cell absorbers. We find that $BaCd_2P_2$ is highly stable in ambient air (for more than 6 months at room temperature) and that immersing

a sample in water for 12 h causes no appreciable changes in the PXRD pattern. Besides, $BaCd_2P_2$ is also found to be resistant to 2.5 M KOH solution for at least 72 h, probably due to passivation of the surface with hydroxide, as indicated by the appearance of a small PXRD peak at 29° (2θ) corresponding to $Cd(OH)_2$ (Figure 4B). Only strong acids, such as HCl, concentrated HNO_3, and *aqua regia*, can dissolve $BaCd_2P_2$. The PXRD pattern of $BaCd_2P_2$ after heating in the open air at 300°C shows no significant change in crystal structure (Figure 4B). PXRD taken after a flow test in N_2 gas reveals the sample to be stable even at 600°C. In a vacuum (i.e., in an evacuated and sealed ampoule), annealing at temperatures of up to 1,100°C results in no changes, attested to by the similar PXRD patterns. During thermogravimetric analysis (TGA) and differential scanning calorimetry (DSC) in an ambient atmosphere, $BaCd_2P_2$ does not show any appreciable change until 425°C, after which the material starts to oxidize (Figures 4C, S10, and S11). Morphology and overall stoichiometry of the synthesized $BaCd_2P_2$ are examined using scanning electron microscopy (SEM) and electron-dispersive X-ray spectroscopy (EDS) (Figures 4D, S12, and S13). The EDS analysis reveals a nearly stoichiometric $BaCd_2P_2$ sample and, importantly, no impurity phases in the sample. Overall, all these results demonstrate a very stable $BaCd_2P_2$ material for which oxidation is probably kinetically limited and which should not require complex encapsulation and cumbersome processing.

PL and carrier lifetime in $BaCd_2P_2$ powder

We have performed optoelectronic characterization of the $BaCd_2P_2$ powder samples. PL spectra are collected using a micro-PL setup in air, which allows us to target individual grains and conduct a statistical analysis of the PL intensity (see details in Note S7). Figure 5A shows a pronounced PL peak at 1.46 eV (847 nm) at 298 K, in very good agreement with the HSE band gap (1.45 eV) as well as the step in the transmittance spectra of $BaCd_2P_2$ (shown in the same figure). This suggests that the PL peak at 1.46 eV is due to band-to-band radiative recombination. A weaker PL peak at 1.27 eV (980 nm) is also observed, probably due to a shallow defect level close to the band edge. Characterizing this second peak will be the focus of our future work. Notably, the intensity of the PL peaks only slightly decreases when the sample is heated up to 368 K and is fully recovered upon cooling back to 298 K (Figure 5A). The robust and strong PL spectra confirm that $BaCd_2P_2$ is also highly stable in terms of its optoelectronic properties in the entire temperature range of 298–323 K for typical solar cell operation.[105]

To assess the PL efficiency more quantitatively and benchmark it versus a well-studied solar absorber material, we compare in Figure 5B the PL spectra of $BaCd_2P_2$ and GaAs powders under identical excitation conditions. The GaAs sample is obtained by pulverizing a piece of prime-grade single-crystal GaAs (001) wafer into a fine powder. GaAs is chosen because it is a well-established, high-efficiency solar absorber and has a similar band gap. The $BaCd_2P_2$ and GaAs powder samples have similar particle sizes (Figure S14), so we expect comparable degrees of surface recombination and multiple scattering optical losses in both samples. Remarkably, Figure 5B shows that the PL peak intensity of our unoptimized $BaCd_2P_2$ sample is already in the same order as that of the GaAs sample (i.e., only ~3 times weaker). This is also clearly seen in Figure 5B inset, which shows the statistical histograms for the 100 random spots on each sample. The result is encouraging because $BaCd_2P_2$, as a new solar absorber material, lacks the level of purity of the prime GaAs wafer.

For a more quantitative study of carrier transport and excited-state dynamics in $BaCd_2P_2$, we have performed time-resolved and steady-state microwave conductivity (TRMC[106–109] and SSMC[110]) measurements on $BaCd_2P_2$ powder (see Note S8).

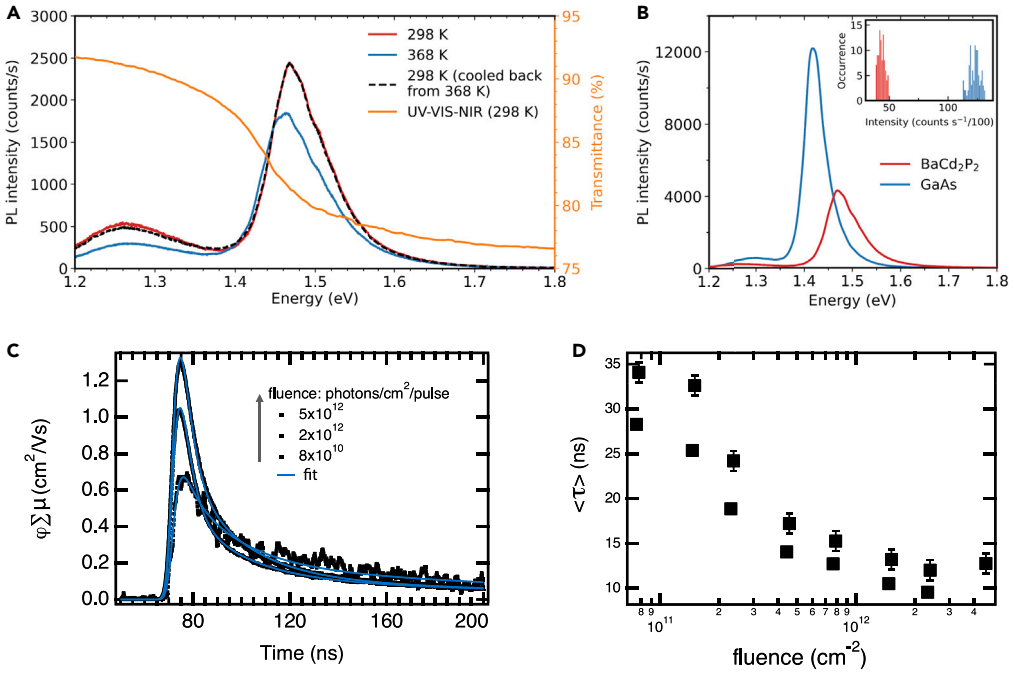

Figure 5. Photoluminescence (PL) and microwave conductivity measurements of $BaCd_2P_2$ polycrystalline samples

(A) Comparison between PL spectra at 298 and 368 K and after cooling down the sample from 368 K back to 298 K.

(B) Average micro-PL spectra of $BaCd_2P_2$ powder versus that of GaAs powder. The inset histograms count the occurrence of the PL intensity across the powders.

(C) Three representative photoconductivity transients (black) and tri-exponential fits (blue) as a function of laser fluence (600 nm and 7 ns FWHM), expressed as the product of carrier yield (φ) and mobility sum ($\sum\mu$).

(D) Population-weighted average carrier lifetime $\langle\tau\rangle$ extracted from the tri-exponential fit to all transients collected for two sample replicates as a function of incident laser fluence.

Microwave conductivity measurements employ a microwave field to probe the conductive and dielectric properties of semiconductor materials without the need for electrical contacts, making them particularly suitable for characterizing powder samples of emerging materials before high-quality thin films are available. Here, we analyze the equilibrium (i.e., dark) properties of the $BaCd_2P_2$ powder (Figure S15A), its transient carrier dynamics (Figures 5C, 5D, and S15B), and its photoconductivity action spectrum (Figure S16). Figure 5C shows photoconductivity transients expressed as a product of charge carrier yield and mobility sum for three representative laser fluences (see also Figure S15B). The solid blue lines show a fit to the data employing three exponential decay components from which the population-weighted average carrier lifetime is calculated. As seen in Figure 5D, the carrier lifetime is within 10–30 ns, depending on fluence; lower fluences result in longer lifetimes. An up to 30-ns photoconductivity lifetime is promising for unoptimized $BaCd_2P_2$ powders because the surface recombination effects are likely at play. For comparison, such a carrier lifetime already exceeds those measured for CdTe (before 2014)[111] and CZTS (present) thin films.[112] Even lead halide perovskites, which are well known for their long carrier lifetimes, started with carrier lifetimes of a few to a few hundred ns measured in thin films.[113,114] As discussed above, carrier lifetime is strongly correlated with the efficiency potential and prospects of a new solar cell absorber.

The yield-mobility product extracted from TRMC provides a weighted sum of the electron and hole mobilities,[106–109] assuming that every absorbed photon creates

an unbound electron-hole pair ($\varphi = 1$). Here, we calculate its value using the sum of the pre-exponential factors from the fits in Figure 5C so as to account for the recombination that occurs within the instrument response function.[115] These values are also fluence dependent. Interestingly, the yield-mobility product *increases* with fluence, from 1 cm^2/Vs at the lowest fluence to 4 cm^2/Vs at the highest fluence (see Figure S15B). Similar behavior is observed in steady-state photo-modulation (Figure S16B), where photoconductivity rises superlinearly ($\Delta\sigma \propto F^{1.5}$) with light flux ($F$). Under most circumstances, the steady-state photoconductivity is expected to be either linear (first-order recombination) or sublinear ($\Delta\sigma \propto F^{0.5}$ for bimolecular recombination). Both our observations suggest that the present mobility and lifetime results are limited by a significant population of trap sites: as the injection density increases and traps become filled, the average carrier mobility increases.[116] This observation could be associated with the high surface area of the powder under investigation (Figure 4D inset). The steady-state photoconductivity action spectra (Figure S16A) and the PL spectra (Figure 5A) are consistent with this surface trap hypothesis. The former exhibits a non-zero tail to the red of the evident absorption onset near 855 nm (i.e., 1.45 eV), and the latter shows a broad second emission peak in the same region.

Finally, we note that the $BaCd_2P_2$ powder measured by TRMC has an XRD coherence length of only ~100 nm (Note S4), which likely suggests that the microwave frequency-dependent mobilities reported above are severely limited by scattering effects due to crystalline grain boundaries or extended structural defects. Indeed, using a confinement length of 100 nm and an observed 9.6-GHz mobility of 4 cm^2/Vs, we get an intrinsic mobility of ~100 cm^2/Vs (Figure S17), in agreement with the computed mobilities. It is worth noting that in the early-stage development of halide perovskite solar cells, the carrier mobilities in $MAPI_3$ were also within the order of magnitude measured for $BaCd_2P_2$ but increased with improvements in film quality.[117]

DISCUSSION

All our computational and experimental results indicate that $BaCd_2P_2$ is a promising solar absorber material for single-junction solar cells. It combines an optimal band gap (1.45 eV) with good transport properties and its measured carrier lifetime on unoptimized powder is high (up to 30 ns). Critical to large-scale PV deployment, $BaCd_2P_2$ does not contain any critical elements and shows high stability in air and water. At this early stage, we can already compare $BaCd_2P_2$ to other thin-film absorber materials. No established thin-film absorbers possess $BaCd_2P_2$'s combination of long carrier lifetime, earth-abundance (outperforming CdTe and CIGS), and high stability (outperforming the halide perovskites). The toxicity of Cd is a legitimate concern, as for Pb in the halide perovskites,[111,118–120] but the element toxicity has so far not stopped the development of either CdTe or halide perovskite solar cells. From previous studies of CdTe solar cells, it has become clear that the toxicity risks can be properly managed by PV module end-of-life recapture and recycling of Cd.[111] Additionally, we note that several other Zintl phosphides crystallize in the same structure as $BaCd_2P_2$, including the less-toxic $CaZn_2P_2$ and $SrZn_2P_2$.[121] In view of the exceptional properties exhibited by $BaCd_2P_2$, these Zn-based compounds are of interest for future studies and could directly eliminate the toxicity concerns.

Although $BaCd_2P_2$ shows promising properties, its future development into a commercial thin-film PV technology will require many additional steps: from growing thin

films (rather than powder) to integrating these films into devices. Thankfully, all of the constituent elements of $BaCd_2P_2$ are already utilized in commercial optoelectronic thin-film technologies.[111,122–124] In view of the long carrier lifetime, even at the powder level, polycrystalline $BaCd_2P_2$ films may be sufficient for high solar cell performance. The early data thus encourage future work to develop low-cost thin-film growth methods, such as physical vapor deposition followed by phosphorization or vapor-transport deposition (VTD).[111,124–128] In addition, the development of lab-scale thin film growth methods that do not often transfer to large-scale PV manufacturing should also be encouraged as necessary to understanding the materials and developing the technology. Such lab-scale methods could include, for example, nanocrystal condensation or pulsed laser deposition.[129–131]

As far as devices are concerned, based on the band gap and predicted dopability of $BaCd_2P_2$, we suggest targeting a single-junction solar cell adopting either a p-n or p-i-n junction device architecture, with $BaCd_2P_2$ used as a p-type or intrinsic absorber layer, respectively. This would require suitable n-type buffer layers (for p-n junction) and hole- and electron-selective layers (for p-i-n junction). Once a $BaCd_2P_2$ solar cell is achieved, long-term device performance and durability under varying environmental conditions should be explored, though our results already show highly stable $BaCd_2P_2$ materials and robust PL under heating. Further down the road, the Zintl AM_2X_2 pnictide family offers band-gap-tuning opportunities through chemical substitution, which would open the door to the use of these Zintl-based materials for tandem cells.

Along the journey toward the development of a new solar cell technology, there will also be unexpected challenges. However, the recent rise of halide perovskites has demonstrated that, with the right material and significant efforts from the community, new solar cell absorbers can be developed entirely from scratch and rapidly reach commercially attractive performance. Although not guaranteed, this makes us hopeful that $BaCd_2P_2$ and other Zintl-based materials in general could emerge as a new thin-film PV technology in the coming years.

Conclusions

We have computationally screened about 40,000 materials searching for high-efficiency, stable, and low-cost thin-film solar cell absorbers. A handful of solar absorber candidates have emerged, and among them, $BaCd_2P_2$ stands out for its computed direct band gap (1.45 eV), high carrier mobilities, large optical absorption coefficients, and, most importantly, favorable point defects that will not lead to strong nonradiative carrier recombination. $BaCd_2P_2$ is also made of low-cost and non-critical elements. Carrier capture calculations show that P_{Cd} is the dominant nonradiative recombination center, but its high formation energy leads to a very long nonradiative lifetime, at least two orders of magnitude higher than that of $MAPI_3$.

Our synthesized $BaCd_2P_2$ powder samples show an experimental band gap in good agreement with theory and exhibit bright PL on par with the luminescence of a high-purity GaAs wafer powder. TRMC measurements on unoptimized powder indicate a carrier lifetime of up to 30 ns, which surpasses early halide perovskites' thin films and is on par with present-day established inorganic PV absorbers. This experimentally confirms the promise of $BaCd_2P_2$ as a new thin-film solar absorber. In addition to its exceptional optoelectronic and defect properties, $BaCd_2P_2$ shows extremely high stability in air and water. It is stable in ambient air for more than 6 months at room temperature, and oxidation only starts for temperatures above 425°C. The high stability will benefit the future development of $BaCd_2P_2$ solar cells.

Beyond $BaCd_2P_2$, our work highlights how HT computational screening, including point-defect properties and follow-up experimental synthesis and characterizations, can identify unexpected solar absorbers with exceptional intrinsic PV properties among tens of thousands of materials. It paves the way for more computation-driven materials discovery in the PV field.

EXPERIMENTAL PROCEDURES

Resource availability

Lead contact

Further information and requests for resources and materials should be directed to and will be fulfilled by the lead contact, Geoffroy Hautier (geoffroy.hautier@dartmouth.edu).

Materials availability

This study did not generate new unique materials.

Data and code availability

All data are present in the paper and supplemental information. Other data are available from the lead contact or corresponding author. Full details of experimental procedures can be found in the supplemental information.

SUPPLEMENTAL INFORMATION

Supplemental information can be found online at https://doi.org/10.1016/j.joule.2024.02.017.

ACKNOWLEDGMENTS

This work was supported by the U.S. Department of Energy, Office of Science, Basic Energy Sciences, Division of Materials Science and Engineering, Physical Behavior of Materials program under award number DE-SC0023509 to Dartmouth and was authored in part by the National Renewable Energy Laboratory, operated by Alliance for Sustainable Energy, LLC, for the U.S. Department of Energy (DOE) under contract no. DE-AC36-08GO28308. All computations, syntheses, and characterizations were supported by this award unless specifically stated otherwise. This research used resources of the National Energy Research Scientific Computing Center (NERSC), a DOE Office of Science User Facility supported by the Office of Science of the U.S. Department of Energy under contract no. DE-AC02-05CH11231 using NERSC award BES-ERCAP0023830. A.P. acknowledges support from a Department of Education GAANN fellowship. Funding for microwave conductivity measurements and analysis on semiconductor powders is provided by the Materials Chemistry Program, Materials Sciences and Engineering Division, Office of Basic Energy Sciences, U.S. Department of Energy under grant DE-SC0023316. The PPMS instrument used for initial attempts of conductivity measurements was supported by Ames National Laboratory, U.S. Department of Energy, which operates under the contract DE-AC02-07CH11358. The views expressed in the article do not necessarily represent the views of the DOE or the U.S. Government.

AUTHOR CONTRIBUTIONS

D.D., A.P., Z.Y., R.C., C.C., Y.X., G.H., G.-M.R., and I.D. worked on the first principles computations, including HT computations. M.R.H., V.K., P.Y., S.Q., S.B., and K.K. worked on the synthesis, structural, chemical, and stability characterizations. G.K., O.G.R., S.Q., S.B., and J.L. worked on the optoelectronic characterizations. Z.Y.

CellPress

and G.H. prepared the manuscript, with inputs from all co-authors. A.Z., D.P.F., S.B., J.L., K.K., I.D., and G.H. supervised the project.

DECLARATION OF INTERESTS

The authors declare no competing interests.

Received: November 15, 2023
Revised: January 23, 2024
Accepted: February 20, 2024
Published: March 11, 2024

REFERENCES

1. Haegel, N.M., Verlinden, P., Victoria, M., Altermatt, P., Atwater, H., Barnes, T., Breyer, C., Case, C., De Wolf, S., Deline, C., et al. (2023). Photovoltaics at multi-terawatt scale: Waiting is not an option. Science *380*, 39–42.

2. van Sark, W. (2023). Photovoltaics performance monitoring is essential in a 100% renewables-based society. Joule *7*, 1388–1393.

3. Jäger-Waldau, A. (2023). Snapshot of photovoltaics – May 2023. EPJ Photovolt. *14*, 23.

4. Wikoff, H.M., Reese, S.B., and Reese, M.O. (2022). Embodied energy and carbon from the manufacture of cadmium telluride and silicon photovoltaics. Joule *6*, 1710–1725.

5. Weiss, D.N. (2021). Tandem solar cells beyond perovskite-silicon. Joule *5*, 2247–2250.

6. Liang, H., Feng, J., Rodríguez-Gallegos, C.D., Krause, M., Wang, X., Alvianto, E., Guo, R., Liu, H., Kothandaraman, R.K., Carron, R., et al. (2023). 29.9%-efficient, commercially viable perovskite/$CuInSe_2$ thin-film tandem solar cells. Joule *7*, 2859–2872.

7. Neugebohrn, N., Haas, S., Gerber, A., Grimm, M., Nissel, J., Liebers, R., Turan, B., Gehrke, K., and Vehse, M. (2022). Flexible design of building integrated thin-film photovoltaics. Prog. Photovolt.: Res. Appl. *30*, 1188–1197.

8. Green, M.A., Dunlop, E.D., Yoshita, M., Kopidakis, N., Bothe, K., Siefer, G., and Hao, X. (2023). Solar cell efficiency tables (version 62). Prog. Photovolt.: Res. Appl *31*, 651–663.

9. Mallick, R., Li, X., Reich, C., Shan, X., Zhang, W., Nagle, T., Bok, L., Bicakci, E., Rosenblatt, N., Modi, D., et al. (2023). Arsenic-Doped CdSeTe Solar Cells Achieve World Record 22.3% Efficiency. IEEE J. Photovolt. *13*, 510–515.

10. Candelise, C., Winskel, M., and Gross, R. (2012). Implications for CdTe and CIGS technologies production costs of indium and tellurium scarcity. Prog. Photovolt.: Res. Appl. *20*, 816–831.

11. Zhang, Y., Kim, M., Wang, L., Verlinden, P., and Hallam, B. (2021). Design considerations for multi-terawatt scale manufacturing of existing and future photovoltaic technologies: challenges and opportunities related to silver, indium and bismuth consumption. Energy Environ. Sci. *14*, 5587–5610.

12. Zhou, J., Xu, X., Wu, H., Wang, J., Lou, L., Yin, K., Gong, Y., Shi, J., Luo, Y., Li, D., et al. (2023). Control of the phase evolution of kesterite by tuning of the selenium partial pressure for solar cells with 13.8% certified efficiency. Nat. Energy *8*, 526–535.

13. Wang, W., Winkler, M.T., Gunawan, O., Gokmen, T., Todorov, T.K., Zhu, Y., and Mitzi, D.B. (2014). Device Characteristics of CZTSSe Thin-Film Solar Cells with 12.6% Efficiency. Adv. Energy Mater. *4*, 1301465.

14. Son, D.-H., Kim, S.-H., Kim, S.-Y., Kim, Y.-I., Sim, J.-H., Park, S.-N., Jeon, D.-H., Hwang, D.-K., Sung, S.-J., Kang, J.-K., et al. (2019). Effect of solid-H_2S gas reactions on CZTSSe thin film growth and photovoltaic properties of a 12.62% efficiency device. J. Mater. Chem. A *7*, 25279–25289.

15. Zhao, Y., Ma, F., Qu, Z., Yu, S., Shen, T., Deng, H.X., Chu, X., Peng, X., Yuan, Y., Zhang, X., and You, J. (2022). Inactive $(PbI_2)_2RbCl$ stabilizes perovskite films for efficient solar cells. Science *377*, 531–534.

16. Stoumpos, C.C., Malliakas, C.D., and Kanatzidis, M.G. (2013). Semiconducting Tin and Lead Iodide Perovskites with Organic Cations: Phase Transitions, High Mobilities, and Near-Infrared Photoluminescent Properties. Inorg. Chem. *52*, 9019–9038.

17. Conings, B., Drijkoningen, J., Gauquelin, N., Babayigit, A., D'Haen, J., D'Olieslaeger, L., Ethirajan, A., Verbeeck, J., Manca, J., Mosconi, E., et al. (2015). Intrinsic Thermal Instability of Methylammonium Lead Trihalide Perovskite. Adv. Energy Mater. *5*, 1500477.

18. Meng, L., You, J., and Yang, Y. (2018). Addressing the stability issue of perovskite solar cells for commercial applications. Nat. Commun. *9*, 5265.

19. Ono, L.K., Qi, Y., and Liu, S. (2018). Progress toward Stable Lead Halide Perovskite Solar Cells. Joule *2*, 1961–1990.

20. Ju, M.-G., Chen, M., Zhou, Y., Dai, J., Ma, L., Padture, N.P., and Zeng, X.C. (2018). Toward Eco-friendly and Stable Perovskite Materials for Photovoltaics. Joule *2*, 1231–1241.

21. Polman, A., Knight, M., Garnett, E.C., Ehrler, B., and Sinke, W.C. (2016). Photovoltaic materials: Present efficiencies and future challenges. Science *352*, aad4424.

22. Zakutayev, A., Major, J.D., Hao, X., Walsh, A., Tang, J., Todorov, T.K., Wong, L.H., and Saucedo, E. (2021). Emerging inorganic solar cell efficiency tables (version 2). J. Phys. Energy *3*. 032003.

23. Zakutayev, A. (2017). Brief review of emerging photovoltaic absorbers. Curr. Opin. Green Sustain. Chem. *4*, 8–15.

24. Hadke, S., Huang, M., Chen, C., Tay, Y.F., Chen, S., Tang, J., and Wong, L. (2022). Emerging Chalcogenide Thin Films for Solar Energy Harvesting Devices. Chem. Rev. *122*, 10170–10265.

25. Choi, J.W., Shin, B., Gorai, P., Hoye, R.L.Z., and Palgrave, R. (2022). Emerging Earth-Abundant Solar Absorbers. ACS Energy Lett. *7*, 1553–1557.

26. Saparov, B. (2022). Next Generation Thin-Film Solar Absorbers Based on Chalcogenides. Chem. Rev. *122*, 10575–10577.

27. Blakesley, J.C., Bonilla, R.S., Freitag, M., Ganose, A.M., Gasparini, N., Kaienburg, P., Koutsourakis, G., Major, J.D., Nelson, J., and Noel, N.K. (2023). Roadmap on Photovoltaic Absorber Materials for Sustainable Energy Conversion. Preprint at arXiv.

28. Wang, A., He, M., Green, M.A., Sun, K., and Hao, X. (2023). A Critical Review on the Progress of Kesterite Solar Cells: Current Strategies and Insights. Adv. Energy Mater. *13*, 2203046.

29. Giraldo, S., Jehl, Z., Placidi, M., Izquierdo-Roca, V., Pérez-Rodríguez, A., and Saucedo, E. (2019). Progress and Perspectives of Thin Film Kesterite Photovoltaic Technology: A Critical Review. Adv. Mater. *31*, e1806692.

30. Gershon, T., Lee, Y.S., Antunez, P., Mankad, R., Singh, S., Bishop, D., Gunawan, O., Hopstaken, M., and Haight, R. (2016). Photovoltaic Materials and Devices Based on the Alloyed Kesterite Absorber $(Ag_xCu_{1-x})_2ZnSnSe_4$. Adv. Energy Mater. *6*, 1502468.

31. Qi, Y.-F., Kou, D.-X., Zhou, W.-H., Zhou, Z.-J., Tian, Q.-W., Meng, Y.-N., Liu, X.-S., Z.-L., Du, and Wu, S.-X. (2017). Engineering of interface band bending and defects elimination via a Ag-graded active layer for efficient $(Cu,Ag)_2ZnSn(S,Se)_4$ solar cells. Energy Environ. Sci. *10*, 2401–2410.

32. Su, Z., Liang, G., Fan, P., Luo, J., Zheng, Z., Xie, Z., Wang, W., Chen, S., Hu, J., Wei, Y., et al. (2020). Device Postannealing Enabling over

12% Efficient Solution-Processed Cu_2ZnSnS_4 Solar Cells with Cd^{2+} Substitution. Adv. Mater. *32*, e2000121.

33. Saliba, M., Matsui, T., Seo, J.-Y., Domanski, K., Correa-Baena, J.-P., Nazeeruddin, M.K., Zakeeruddin, S.M., Tress, W., Abate, A., Hagfeldt, A., and Grätzel, M. (2016). Cesium-containing triple cation perovskite solar cells: improved stability, reproducibility and high efficiency. Energy Environ. Sci. *9*, 1989–1997.

34. Gratia, P., Grancini, G., Audinot, J.N., Jeanbourquin, X., Mosconi, E., Zimmermann, I., Dowsett, D., Lee, Y., Grätzel, M., De Angelis, F., et al. (2016). Intrinsic Halide Segregation at Nanometer Scale Determines the High Efficiency of Mixed Cation/Mixed Halide Perovskite Solar Cells. J. Am. Chem. Soc. *138*, 15821–15824.

35. McMeekin, D.P., Sadoughi, G., Rehman, W., Eperon, G.E., Saliba, M., Hörantner, M.T., Haghighirad, A., Sakai, N., Korte, L., Rech, B., et al. (2016). A mixed-cation lead mixed-halide perovskite absorber for tandem solar cells. Science *351*, 151–155.

36. Lee, J.W., Tan, S., Seok, S.I., Yang, Y., and Park, N.G. (2022). Rethinking the A cation in halide perovskites. Science *375*, eabj1186.

37. Yu, L., and Zunger, A. (2012). Identification of Potential Photovoltaic Absorbers Based on First-Principles Spectroscopic Screening of Materials. Phys. Rev. Lett. *108*. 068701.

38. Körbel, S., Marques, M.A.L., and Botti, S. (2016). Stability and electronic properties of new inorganic perovskites from high-throughput ab initio calculations. J. Mater. Chem. C *4*, 3157–3167.

39. Chakraborty, S., Xie, W., Mathews, N., Sherburne, M., Ahuja, R., Asta, M., and Mhaisalkar, S.G. (2017). Rational Design: A High-Throughput Computational Screening and Experimental Validation Methodology for Lead-Free and Emergent Hybrid Perovskites. ACS Energy Lett. *2*, 837–845.

40. Zhao, X.-G., Yang, J.-H., Fu, Y., Yang, D., Xu, Q., Yu, L., Wei, S.-H., and Zhang, L. (2017). Design of Lead-Free Inorganic Halide Perovskites for Solar Cells via Cation-Transmutation. J. Am. Chem. Soc. *139*, 2630–2638.

41. Huo, Z., Wei, S.-H., and Yin, W.-J. (2018). High-throughput screening of chalcogenide single perovskites by first-principles calculations for photovoltaics. J. Phys. D *51*, 474003.

42. Kuhar, K., Pandey, M., Thygesen, K.S., and Jacobsen, K.W. (2018). High-Throughput Computational Assessment of Previously Synthesized Semiconductors for Photovoltaic and Photoelectrochemical Devices. ACS Energy Lett. *3*, 436–446.

43. Fabini, D.H., Koerner, M., and Seshadri, R. (2019). Candidate Inorganic Photovoltaic Materials from Electronic Structure-Based Optical Absorption and Charge Transport Proxies. Chem. Mater. *31*, 1561–1574.

44. Kang, Y., Youn, Y., Han, S., Park, J., and Oh, C.-S. (2019). Computational Screening of Indirect-Gap Semiconductors for Potential Photovoltaic Absorbers. Chem. Mater. *31*, 4072–4080.

45. Cai, Y., Xie, W., Teng, Y.T., Harikesh, P.C., Ghosh, B., Huck, P., Persson, K.A., Mathews, N., Mhaisalkar, S.G., Sherburne, M., and Asta, M. (2019). High-throughput Computational Study of Halide Double Perovskite Inorganic Compounds. Chem. Mater. *31*, 5392–5401.

46. Li, Y., and Yang, K. (2019). High-throughput computational design of organic–inorganic hybrid halide semiconductors beyond perovskites for optoelectronics. Energy Environ. Sci. *12*, 2233–2243.

47. Dahliah, D., Brunin, G., George, J., Ha, V.-A., Rignanese, G.-M., and Hautier, G. (2021). High-throughput computational search for high carrier lifetime, defect-tolerant solar absorbers. Energy Environ. Sci. *14*, 5057–5073.

48. Mannodi-Kanakkithodi, A., and Chan, M.K.Y. (2022). Data-driven design of novel halide perovskite alloys. Energy Environ. Sci. *15*, 1930–1949.

49. Jaramillo, R., Sher, M.-J., Ofori-Okai, B.K., Steinmann, V., Yang, C., Hartman, K., Nelson, K.A., Lindenberg, A.M., Gordon, R.G., and Buonassisi, T. (2016). Transient terahertz photoconductivity measurements of minority-carrier lifetime in tin sulfide thin films: Advanced metrology for an early stage photovoltaic material. J. Appl. Phys. *119*. 035101.

50. Brandt, R.E., Stevanović, V., Ginley, D.S., and Buonassisi, T. (2015). Identifying defect-tolerant semiconductors with high minority-carrier lifetimes: beyond hybrid lead halide perovskites. MRS Commun. *5*, 265–275.

51. Zakutayev, A., Caskey, C.M., Fioretti, A.N., Ginley, D.S., Vidal, J., Stevanovic, V., Tea, E., and Lany, S. (2014). Defect Tolerant Semiconductors for Solar Energy Conversion. J. Phys. Chem. Lett. *5*, 1117–1125.

52. Brandt, R.E., Poindexter, J.R., Gorai, P., Kurchin, R.C., Hoye, R.L.Z., Nienhaus, L., Wilson, M.W.B., Polizzotti, J.A., Sereika, R., Žaltauskas, R., et al. (2017). Searching for "Defect-Tolerant" Photovoltaic Materials: Combined Theoretical and Experimental Screening. Chem. Mater. *29*, 4667–4674.

53. Walsh, A., and Zunger, A. (2017). Instilling defect tolerance in new compounds. Nat. Mater. *16*, 964–967.

54. Park, J.S., Kim, S., Xie, Z., and Walsh, A. (2018). Point defect engineering in thin-film solar cells. Nat. Rev. Mater. *3*, 194–210.

55. Huang, Y.-T., Kavanagh, S.R., Scanlon, D.O., Walsh, A., and Hoye, R.L.Z. (2021). Perovskite-inspired materials for photovoltaics and beyond—from design to devices. Nanotechnology *32*, 132004.

56. Kumagai, Y., Kavanagh, S.R., Suzuki, I., Omata, T., Walsh, A., Scanlon, D.O., and Morito, H. (2023). Alkali Mono-Pnictides: A New Class of Photovoltaic Materials by Element Mutation. PRX Energy *2*. 043002.

57. Jain, A., Ong, S.P., Hautier, G., Chen, W., Richards, W.D., Dacek, S., Cholia, S., Gunter, D., Skinner, D., Ceder, G., and Persson, K.A. (2013). Commentary: The Materials Project: A materials genome approach to accelerating materials innovation. APL Mater. *1*. 011002.

58. Bergerhoff, G., Hundt, R., Sievers, R., and Brown, I.D. (1983). The inorganic crystal structure data base. J. Chem. Inf. Comput. Sci. *23*, 66–69.

59. Heyd, J., Scuseria, G.E., and Ernzerhof, M. (2006). Erratum: "Hybrid functionals based on a screened Coulomb potential" [J. Chem. Phys. 118, 8207 (2003)]. J. Chem. Phys. *124*, 219906.

60. Kirchartz, T., and Rau, U. (2018). What Makes a Good Solar Cell? Adv. Energy Mater. *8*, 1703385.

61. Guillemoles, J.-F., Kirchartz, T., Cahen, D., and Rau, U. (2019). Guide for the perplexed to the Shockley–Queisser model for solar cells. Nat. Photonics *13*, 501–505.

62. Kim, S., Márquez, J.A., Unold, T., and Walsh, A. (2020). Upper limit to the photovoltaic efficiency of imperfect crystals from first principles. Energy Environ. Sci. *13*, 1481–1491.

63. Bartel, C.J. (2022). Review of computational approaches to predict the thermodynamic stability of inorganic solids. J. Mater. Sci. *57*, 10475–10498.

64. Tolborg, K., Klarbring, J., Ganose, A.M., and Walsh, A. (2022). Free energy predictions for crystal stability and synthesisability. Digit. Disc *1*, 586–595.

65. Twyman, N.M., Walsh, A., and Buonassisi, T. (2022). Environmental Stability of Crystals: A Greedy Screening. Chem. Mater. *34*, 2545–2552.

66. Sopiha, K.V., Comparotto, C., Márquez, J.A., and Scragg, J.J.S. (2022). Chalcogenide Perovskites: Tantalizing Prospects, Challenging Materials. Adv. Opt. Mater. *10*, 2101704.

67. Sun, Y.-Y., Agiorgousis, M.L., Zhang, P., and Zhang, S. (2015). Chalcogenide Perovskites for Photovoltaics. Nano Lett. *15*, 581–585.

68. Klüfers, P., Neumann, H., Mewis, A., and Schuster, H.-U. (1980). AB_2X_2-Verbindungen im $CaAl_2Si_2$-Typ, VIII [1] / AB_2X_2 Compounds with the $CaAl_2Si_2$ Structure, VIII [1]. Z. Naturforsch. B *35*, 1317–1318.

69. Liu, D., Peng, H., Huang, J., and Sa, R. (2022). Revealing the stability and optoelectronic properties of novel nitride and phosphide semiconductors: A DFT prediction. Surf. Interfaces *29*, 101740.

70. Savelsberg, G. (1978). Ternäre Pnictide und Chalkogenide von Alkalimetallen und IB-bzw. IIB-Elementen / On Ternary Pnictides and Chalkogenides of Alkaline Metals and IB- resp. II B-Elements. Z. Naturforsch. B *33*, 370–373.

71. McCarroll, W.H., and Simon, R.E. (1964). Simple Electron Diffraction Camera for the Examination of Alkali Antimonide Photoelectric Films. Rev. Sci. Instrum. *35*, 508–511.

72. Antoniuk, E.R., Schindler, P., Schroeder, W.A., Dunham, B., Pianetta, P., Vecchione, T., and Reed, E.J. (2021). Novel Ultrabright and Air-Stable Photocathodes Discovered from Machine Learning and Density Functional Theory Driven Screening. Adv. Mater. *33*, e2104081.

73. DiSalvo, F.J., Trail, S.S., Yamane, H., and Brese, N.E. (1997). The crystal structure of $Sr_6Cu_3N_5$ with isolated, bent $(Cu_2{}^1N_3)^{7-}$ anions and the single crystal structural determination of SrCuN. J. Alloys Compd. *255*, 122–129.

74. Chern, M.Y., Disalvo, F.J., Parise, J.B., and Goldstone, J.A. (1992). The structural distortion of the anti-perovskite nitride Ca_3AsN. J. Solid State Chem. *96*, 426–435.

75. Zheng, C., Hoffmann, R., Nesper, R., and Von Schnering, H.G. (1986). Site preferences and bond length differences in $CaAl_2Si_2$-type Zintl compounds. J. Am. Chem. Soc. *108*, 1876–1884.

76. Peng, W., Petretto, G., Rignanese, G.-M., Hautier, G., and Zevalkink, A. (2018). An Unlikely Route to Low Lattice Thermal Conductivity: Small Atoms in a Simple Layered Structure. Joule *2*, 1879–1893.

77. Wang, T., Daiber, B., Frost, J.M., Mann, S.A., Garnett, E.C., Walsh, A., and Ehrler, B. (2017). Indirect to direct bandgap transition in methylammonium lead halide perovskite. Energy Environ. Sci. *10*, 509–515.

78. Ricci, F., Chen, W., Aydemir, U., Snyder, G.J., Rignanese, G.-M., Jain, A., and Hautier, G. (2017). An ab initio electronic transport database for inorganic materials. Sci. Data *4*, 170085.

79. Vukmirović, N. (2021). Calculations of electron mobility in II-VI semiconductors. Phys. Rev. B *104*. 085203.

80. Ganose, A.M., Park, J., Faghaninia, A., Woods-Robinson, R., Persson, K.A., and Jain, A. (2021). Efficient calculation of carrier scattering rates from first principles. Nat. Commun. *12*, 2222.

81. Monserrat, B., Park, J.-S., Kim, S., and Walsh, A. (2018). Role of electron-phonon coupling and thermal expansion on band gaps, carrier mobility, and interfacial offsets in kesterite thin-film solar cells. Appl. Phys. Lett. *112*, 193903.

82. Poncé, S., Li, W., Reichardt, S., and Giustino, F. (2020). First-principles calculations of charge carrier mobility and conductivity in bulk semiconductors and two-dimensional materials. Rep. Prog. Phys. *83*. 036501.

83. Yin, W.-J., Shi, T., and Yan, Y. (2014). Unusual defect physics in $CH_3NH_3PbI_3$ perovskite solar cell absorber. Appl. Phys. Lett. *104*. 063903.

84. Buin, A., Comin, R., Xu, J., Ip, A.H., and Sargent, E.H. (2015). Halide-Dependent Electronic Structure of Organolead Perovskite Materials. Chem. Mater. *27*, 4405–4412.

85. Meggiolaro, D., and De Angelis, F. (2018). First-Principles Modeling of Defects in Lead Halide Perovskites: Best Practices and Open Issues. ACS Energy Lett. *3*, 2206–2222.

86. Meggiolaro, D., Motti, S.G., Mosconi, E., Barker, A.J., Ball, J., Andrea Riccardo Perini, C., Deschler, F., Petrozza, A., and De Angelis, F. (2018). Iodine chemistry determines the defect tolerance of lead-halide perovskites. Energy Environ. Sci. *11*, 702–713.

87. Keeble, D.J., Wiktor, J., Pathak, S.K., Phillips, L.J., Dickmann, M., Durose, K., Snaith, H.J., and Egger, W. (2021). Identification of lead vacancy defects in lead halide perovskites. Nat. Commun. *12*, 5566.

88. Lyons, J.L., and Swift, M.W. (2023). Trends for Acceptor Dopants in Lead Halide Perovskites. J. Phys. Chem. C *127*, 12735–12740.

89. Zhang, S.B., Wei, S.-H., Zunger, A., and Katayama-Yoshida, H. (1998). Defect physics of the $CuInSe_2$ chalcopyrite semiconductor. Phys. Rev. B *57*, 9642–9656.

90. Freysoldt, C., Grabowski, B., Hickel, T., Neugebauer, J., Kresse, G., Janotti, A., and Van de Walle, C.G. (2014). First-principles calculations for point defects in solids. Rev. Mod. Phys. *86*, 253–305.

91. Liu, J., Song, Y., Xu, X., Li, W., Yang, J., and Li, X. (2023). Identification of intrinsic defects and hydrogen passivation in InP using hybrid functional. J. Appl. Phys. *134*, 115702.

92. Yuan, Z., Xiong, Y., and Hautier, G. (2023). First-principles study of intrinsic and hydrogen point defects in the earth-abundant photovoltaic absorber Zn_3P_2. J. Mater. Chem. A *11*, 20592–20600.

93. Zhang, S.B., Wei, S.-H., and Zunger, A. (1998). A phenomenological model for systematization and prediction of doping limits in II–VI and I–III–VI_2 compounds. J. Appl. Phys. *83*, 3192–3196.

94. Robertson, J., and Clark, S.J. (2011). Limits to doping in oxides. Phys. Rev. B *83*. 075205.

95. Alkauskas, A., Yan, Q., and Van de Walle, C.G. (2014). First-principles theory of nonradiative carrier capture via multiphonon emission. Phys. Rev. B *90*. 075202.

96. Li, J., Zhu, H.-F., Zhang, Y.-Y., Yuan, Z.-K., Chen, S., and Gong, X.-G. (2017). Large carrier-capture rate of Pb_I antisite in $CH_3NH_3PbI_3$ induced by heavy atoms and soft phonon modes. Phys. Rev. B *96*, 104103.

97. Zhang, X., Turiansky, M.E., Shen, J.-X., and Van de Walle, C.G. (2022). Defect tolerance in halide perovskites: A first-principles perspective. J. Appl. Phys. *131*. 090901.

98. Bagraev, N.T., and Mashkov, V.A. (1988). A mechanism for two-electron capture at deep level defects in semiconductors. Solid State Commun. *65*, 1111–1117.

99. Zhang, X., Turiansky, M.E., Shen, J.-X., and Van de Walle, C.G. (2020). Iodine interstitials as a cause of nonradiative recombination in hybrid perovskites. Phys. Rev. B *101*, 140101.

100. Yang, J.-H., Yin, W.-J., Park, J.-S., Ma, J., and Wei, S.-H. (2016). Review on first-principles study of defect properties of CdTe as a solar cell absorber. Semicond. Sci. Technol. *31*. 083002.

101. Kavanagh, S.R., Walsh, A., and Scanlon, D.O. (2021). Rapid Recombination by Cadmium Vacancies in CdTe. ACS Energy Lett. *6*, 1392–1398.

102. Dou, B., Falletta, S., Neugebauer, J., Freysoldt, C., Zhang, X., and Wei, S.-H. (2023). Chemical Trend of Nonradiative Recombination in Cu(In,Ga)Se_2 Alloys. Phys. Rev. Appl. *19*. 054054.

103. Li, J., Yuan, Z.-K., Chen, S., Gong, X.-G., and Wei, S.-H. (2019). Effective and Noneffective Recombination Center Defects in Cu_2ZnSnS_4: Significant Difference in Carrier Capture Cross Sections. Chem. Mater. *31*, 826–833.

104. Kim, S., Park, J.-S., Hood, S.N., and Walsh, A. (2019). Lone-pair effect on carrier capture in Cu_2ZnSnS_4 solar cells. J. Mater. Chem. A *7*, 2686–2693.

105. Singh, P., and Ravindra, N.M. (2012). Temperature dependence of solar cell performance—an analysis. Sol. Energy Mater. Sol. Cells *101*, 36–45.

106. Savenije, T.J., Ferguson, A.J., Kopidakis, N., and Rumbles, G. (2013). Revealing the Dynamics of Charge Carriers in Polymer:Fullerene Blends Using Photoinduced Time-Resolved Microwave Conductivity. J. Phys. Chem. C *117*, 24085–24103.

107. Reid, O.G., Moore, D.T., Li, Z., Zhao, D., Yan, Y., Zhu, K., and Rumbles, G. (2017). Quantitative analysis of time-resolved microwave conductivity data. J. Phys. D *50*, 493002.

108. Hempel, H., Savenjie, T.J., Stolterfoht, M., Neu, J., Failla, M., Paingad, V.C., Kužel, P., Heilweil, E.J., Spies, J.A., Schleuning, M., et al. (2022). Predicting Solar Cell Performance from Terahertz and Microwave Spectroscopy. Adv. Energy Mater. *12*, 2102776.

109. Savenije, T.J., Guo, D., Caselli, V.M., and Hutter, E.M. (2020). Quantifying Charge-Carrier Mobilities and Recombination Rates in Metal Halide Perovskites from Time-Resolved Microwave Photoconductivity Measurements. Adv. Energy Mater. *10*, 1903788.

110. Blackburn, J.L., Zhang, H., Myers, A.R., Dunklin, J.R., Coffey, D.C., Hirsch, R.N., Vigil-Fowler, D., Yun, S.J., Cho, B.W., Lee, Y.H., et al. (2020). Measuring Photoexcited Free Charge Carriers in Mono- to Few-Layer Transition-Metal Dichalcogenides with Steady-State Microwave Conductivity. J. Phys. Chem. Lett. *11*, 99–107.

111. Scarpulla, M.A., McCandless, B., Phillips, A.B., Yan, Y., Heben, M.J., Wolden, C., Xiong, G., Metzger, W.K., Mao, D., Krasikov, D., et al. (2023). CdTe-based thin film photovoltaics: Recent advances, current challenges and future prospects. Sol. Energy Mater. Sol. Cells *255*, 112289.

112. Hempel, H., Dennler, G., Müller, S., Larramona, G., Eichberger, R., and Unold, T. (2016). Charge carrier dynamics in $Cu_2ZnSn(S/Se)_4$ thin film solar cells measured by time resolved terahertz and microwave spectroscopy. In 2016 41st International Conference on Infrared, Millimeter, and Terahertz waves (IRMMW-THz), pp. 1–2.

113. Xing, G., Mathews, N., Sun, S., Lim, S.S., Lam, Y.M., Grätzel, M., Mhaisalkar, S., and Sum, T.C. (2013). Long-Range Balanced Electron- and Hole-Transport Lengths in Organic-Inorganic $CH_3NH_3PbI_3$. Science *342*, 344–347.

114. Stranks, S.D., Eperon, G.E., Grancini, G., Menelaou, C., Alcocer, M.J.P., Leijtens, T., Herz, L.M., Petrozza, A., and Snaith, H.J. (2013). Electron-Hole Diffusion Lengths Exceeding 1 Micrometer in an Organometal

Trihalide Perovskite Absorber. Science *342*, 341–344.

115. Ferguson, A.J., Kopidakis, N., Shaheen, S.E., and Rumbles, G. (2008). Quenching of Excitons by Holes in Poly(3-hexylthiophene) Films. J. Phys. Chem. C *112*, 9865–9871.

116. Kroeze, J.E., Savenije, T.J., and Warman, J.M. (2004). Electrodeless Determination of the Trap Density, Decay Kinetics, and Charge Separation Efficiency of Dye-Sensitized Nanocrystalline TiO_2. J. Am. Chem. Soc. *126*, 7608–7618.

117. Herz, L.M. (2017). Charge-Carrier Mobilities in Metal Halide Perovskites: Fundamental Mechanisms and Limits. ACS Energy Lett. *2*, 1539–1548.

118. Nain, P., and Kumar, A. (2020). Ecological and human health risk assessment of metals leached from end-of-life solar photovoltaics. Environ. Pollut. *267*, 115393.

119. Padture, N.P. (2023). The promise of metal-halide-perovskite solar photovoltaics: A brief review. MRS Bull. *48*, 983–998.

120. Dissanayake, P.D., Yeom, K.M., Sarkar, B., Alessi, D.S., Hou, D., Rinklebe, J., Noh, J.H., and Ok, Y.S. (2023). Environmental impact of metal halide perovskite solar cells and potential mitigation strategies: A critical review. Environ. Res. *219*, 115066.

121. Katsube, R., and Nose, Y. (2022). Synthesis of alkaline-earth Zintl phosphides MZn_2P_2 (M = Ca, Sr, Ba) from Sn solutions. High Temp. Mater. Process *41*, 8–15.

122. Fazlioglu-Yalcin, B., Suceava, A.C., Kuznetsova, T., Wang, K., Gopalan, V., and Engel-Herbert, R. (2023). Stoichiometric Control and Optical Properties of $BaTiO_3$ Thin Films Grown by Hybrid MBE. Adv. Mater. Interfaces *10*, 2300018.

123. Buscaglia, V., Buscaglia, M.T., and Canu, G. (2021). $BaTiO_3$-Based Ceramics: Fundamentals, Properties and Applications. In Encyclopedia of Materials: Technical Ceramics and Glasses, M. Pomeroy, ed. (Elsevier), pp. 311–344.

124. Greenaway, A.L., Boucher, J.W., Oener, S.Z., Funch, C.J., and Boettcher, S.W. (2017). Low-Cost Approaches to III–V Semiconductor Growth for Photovoltaic Applications. ACS Energy Lett. *2*, 2270–2282.

125. Schnepf, R.R., Crovetto, A., Gorai, P., Park, A., Holtz, M., Heinselman, K.N., Bauers, S.R., Brooks Tellekamp, M., Zakutayev, A., Greenaway, A.L., et al. (2022). Reactive phosphine combinatorial co-sputtering of cation disordered $ZnGeP_2$ films. J. Mater. Chem. C *10*, 870–879.

126. Crovetto, A., Adamczyk, J.M., Schnepf, R.R., Perkins, C.L., Hempel, H., Bauers, S.R., Toberer, E.S., Tamboli, A.C., Unold, T., and Zakutayev, A. (2022). Boron Phosphide Films by Reactive Sputtering: Searching for a P-Type Transparent Conductor. Adv. Mater. Interfaces *9*, 2200031.

127. Romeo, A., Terheggen, M., Abou-Ras, D., Bätzner, D.L., Haug, F.-J., Kälin, M., Rudmann, D., and Tiwari, A.N. (2004). Development of thin-film Cu(In,Ga)Se_2 and CdTe solar cells. Prog. Photovolt.: Res. Appl. *12*, 93–111.

128. Hsu, W.-J., Pettit, E.C., Swartwout, R., Kadosh, T., Srinivasan, S., Wassweiler, E., Bulovic, V., and Holmes, R.J. (2023). Vapor transport deposition of metal-halide perovskites solar cells. Organic, Hybrid, and Perovskite Photovoltaics *XXIV*, 1266007.

129. Luber, E.J., Mobarok, M.H., and Buriak, J.M. (2013). Solution-Processed Zinc Phosphide (α-Zn_3P_2) Colloidal Semiconducting Nanocrystals for Thin Film Photovoltaic Applications. ACS Nano *7*, 8136–8146.

130. Surendran, M., Chen, H., Zhao, B., Thind, A.S., Singh, S., Orvis, T., Zhao, H., Han, J.-K., Htoon, H., Kawasaki, M., et al. (2021). Epitaxial Thin Films of a Chalcogenide Perovskite. Chem. Mater. *33*, 7457–7464.

131. Rodkey, N., Kaal, S., Sebastia-Luna, P., Birkhölzer, Y.A., Ledinsky, M., Palazon, F., Bolink, H.J., and Morales-Masis, M. (2021). Pulsed Laser Deposition of $Cs_2AgBiBr_6$: from Mechanochemically Synthesized Powders to Dry, Single-Step Deposition. Chem. Mater. *33*, 7417–7422.